OPTICS

Dynamic thermal emission control with InAs-based plasmonic metasurfaces

Junghyun Park[1]*, Ju-Hyung Kang[1]*, Xiaoge Liu[1], Scott J. Maddox[2], Kechao Tang[1], Paul C. McIntyre[1], Seth R. Bank[2], Mark L. Brongersma[1†]

Thermal emission from objects tends to be spectrally broadband, unpolarized, and temporally invariant. These common notions are now challenged with the emergence of new nanophotonic structures and concepts that afford on-demand, active manipulation of the thermal emission process. This opens a myriad of new applications in chemistry, health care, thermal management, imaging, sensing, and spectroscopy. Here, we theoretically propose and experimentally demonstrate a new approach to actively tailor thermal emission with a reflective, plasmonic metasurface in which the active material and reflector element are epitaxially grown, high-carrier-mobility InAs layers. Electrical gating induces changes in the charge carrier density of the active InAs layer that are translated into large changes in the optical absorption and thermal emission from metasurface. We demonstrate polarization-dependent and electrically controlled emissivity changes of 3.6%P (6.5% in relative scale) in the mid-infrared spectral range.

INTRODUCTION

Thermal sources find extensive use in chemical analysis, gas sensing, thermal imaging, and thermophotovoltaics (*1*–*3*). They primarily emit in the mid-infrared (IR) spectral range, where many gases, liquids, and solids display unique, vibrational absorption features. The dependence of thermal emission on the temperature of an object is by now well established (*4*). However, on-demand control over the thermal emission properties in terms of the spectral content, directionality, and polarization has only been achieved more recently.

The demonstrated ability to use micromachined structures to tailor thermal emission properties (*5*) has prompted considerable efforts to more accurately control this emission with carefully engineered nanostructures (*6*–*8*). Thermal radiation with a high degree of temporal and spatial coherence was also implemented recently using grating couplers (*6*, *7*) and coupled resonant cavities (*8*). This has dispelled many of the conventional beliefs about the nature of thermal emission. Researchers also designed layered materials to effectively reflect light in the visible spectrum and absorb/emit in the mid-IR, leading to new commercial applications in radiative cooling (*9*) or the development of more efficient incandescent light bulbs (*10*). Kirchhoff's law, which states that the emissivity is equal to absorptivity for an object in thermodynamic equilibrium, has played a key role in the design of many of these devices (*11*). With this law, we can leverage recent developments in the design of various nanostructured optical absorber materials (*12*–*14*) to expedite the realization of efficient thermal emitters that display desired emission properties. Within the limitations imposed by Planck's radiation law, the maximum emission could be achieved by implementing perfect absorbers in photonic crystal cavities (*15*, *16*) and metasurfaces (*17*, *18*) through careful impedance matching.

As a next logical step, there is growing interest in devices that afford postfabrication tuning and dynamic tuning of thermal emission (*19*–*25*). A packaged metasurface thermal emitter was combined with a membrane heater to produce a CO_2 sensor (*19*), but the large thermal mass limited the operating speed to around 10 Hz. Microelectromechanical systems–based tuning of the distance between a top antenna and a bottom mirror showed much faster (up to 30 kHz) modulation, with a modulation depth of 56% at 6.2 μm (*17*, *20*). The first electrical modulation of thermal emission in far-IR was demonstrated by Vassant and colleagues (*21*) by tuning the epsilon-near-zero (ENZ) mode in a single AlGaAs/GaAs/AlGaAs quantum well. This work is based on the coupling between an intersubband transition and a surface phonon-polariton resonance, and thus, the ENZ effect is limited to a narrow wavelength range (*22*). Graphene nanoresonators on top of a gold mirror with a quarter-wave spacer of 1-μm SiN_x showed emissivity changes Δε of 0.04 under application of a 60-V electrical bias at 250°C (*23*). Noda and colleagues reported ultrafast dynamic thermal emission control by modulating the intersubband absorption in n-type quantum wells embedded in a photonic crystal cavity, resulting in 600-kHz speed with 10-V electrical bias (*24*, *25*). Thermal emission ranging from 3.5 to 8.0 μm from thin epitaxially grown In(Ga)Sb layers in InAs(Sb) matrices was demonstrated by optically pumping this material with 980-nm pulse laser (*26*).

Here, we present dynamic control over the thermal emission from a plasmonic metasurface. The metasurface is constructed from a dense array of plasmonic cavities, which feature high-performance, epitaxially grown InAs active and reflector layers. We show that charge accumulation and depletion upon electrical gating with 40 V result in emissivity changes around 3.6%P at a wavelength of 7.3 μm. Various advantages of plasmonic metasurfaces such as high-speed operation, polarization selectivity (*27*), ability to achieve individual control of unit pixels (*28*), phase tunability (*28*, *29*), and ENZ strong coupling (*30*) become possible in the proposed configuration to facilitate more versatile tunable thermal emitters.

RESULTS AND DISCUSSION

According to Kirchhoff's law, the emissivity $E(\lambda)$ is equal to the absorptivity $A(\lambda)$ (*11*). The creation of a metasurface with a high, tunable emissivity at a specified target wavelength thus boils down to the engineering of a metasurface with a strong, tunable absorption resonance at that wavelength. Figure 1A shows a cross section of the proposed device configuration that achieves this. It is inspired by previous

[1]Geballe Laboratory for Advanced Materials, Stanford University, Stanford, CA 94305, USA. [2]Microelectronics Research Center and Department of Electrical and Computer Engineering, The University of Texas at Austin, Austin, TX 78758, USA.
*These authors contributed equally to this work.
†Corresponding author. Email: brongersma@stanford.edu

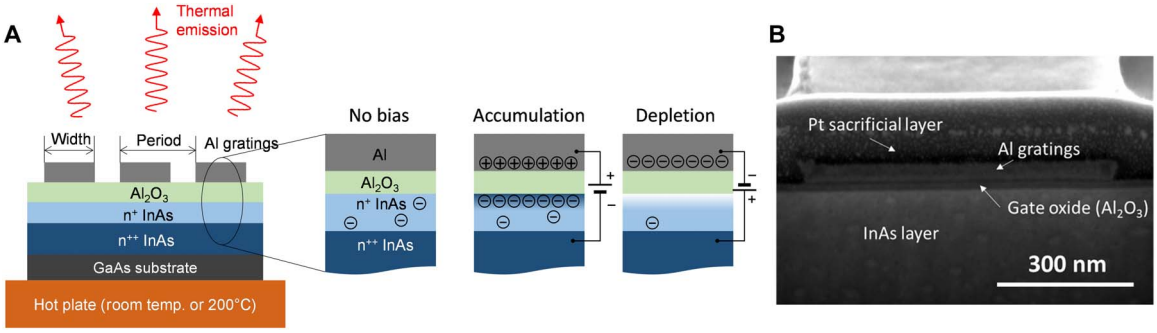

Fig. 1. Configuration of an electrically tunable III-V–based metasurface for dynamic thermal emission control. (**A**) Device schematic of active metasurface. A high-doped (n^{++}) InAs layer is epitaxially grown on top of a GaAs substrate and is used as a metallic mirror with a negative real dielectric constant at the operating wavelength. A low-doped (n^+) InAs layer functions as an active layer whose carrier density and concomitant optical properties can be controlled with an external electrical bias. A thin Al_2O_3 layer serves as both a gate oxide and an optical spacer to a metasurface/grating made from Al strips. These strips form a series of nano-cavities for gap plasmons that can be excited between the strips and a high-doped (n^{++}) InAs mirror. The insets show enlarged schematics for no bias, accumulation, and depletion cases. (**B**) Cross-sectional SEM taken from one of the strip cavities. The thicknesses of the Al strips, the Al_2O_3 gate oxide, the n^+ InAs active layer, and the n^{++} InAs bottom mirror are 50, 30, 50, and 500 nm, respectively. The strip width and period of the metasurface are 700 nm and 1.2 μm, respectively.

work on near-unity light absorbers composed of a dense array of metallic patches or strips above a metallic back reflector. The strips define plasmonic cavities that afford extreme light concentration and absorption through the excitation of gap plasmons (*13*, *27*, *31*). The strips are also used to electrically gate and tune the cavity resonances. The metallic reflector is created by doping a crystalline InAs substrate with Si atoms to produce a mobile electron concentration n of 10^{20} cm^{-3}. This results in a negative-valued real part of the permittivity in the mid-IR range, allowing its operation as a metallic mirror. An InAs layer with a lower doping level ($n = 10^{19}$ cm^{-3}) is epitaxially grown on top of this substrate and serves as the active tuning layer in our device. The InAs layers feature high carrier mobilities of 5×10^2 $cm^2/V{\cdot}s$ for 10^{20} cm^{-3} and 1×10^3 $cm^2/V{\cdot}s$ for 10^{19} cm^{-3} and were grown via surfactant-mediated epitaxy using bismuth. Previous studies on semiconducting oxide–based metasurfaces revealed the effectiveness of using semiconducting active layers to tune the resonant response of plasmonic cavities (*28*, *32*), especially near the ENZ wavelength, where the magnitude of permittivity is near-zero valued (*27*, *30*). The carrier concentration in this work is chosen such that the ENZ point of the active layer occurs at a target wavelength around 7.0 μm, where the doped InAs substrate behaves as an excellent mirror (*33*). The third layer made from Al_2O_3 plays a dual role as an optical spacer and an electric insulator that prevents charge leakage from the InAs layer to the top electrodes. The change in the surface charge density between the gate oxide layer and the low-doped InAs layer will give rise to changes in their resonance condition. Last, we pattern the binary Al grating on top of this stack to finish the devices. Together with the material in the gap, the width of each strip determines the propagation phase of the oscillating gap plasmons in traversing the cavity (*27*, *31*), and thus also the resonance wavelength. Near-unity absorption in this metasurface can be achieved by spacing the cavities at a well-chosen period. At this period, the light flowing through the cavities and the directly reflected light from the reflective surface interfere destructively, and no light can escape the metasurface.

Figure 1B shows the cross-sectional scanning electron microscopy (SEM) image of a fabricated device. The thickness of the top Al strips, the gate oxide, and the low-doped InAs active layer are designed and measured as 50, 30, and 50 nm, respectively. The width of this Al strip is 700 nm, and the strips in this sample are spaced at a period of 1.2 μm. We also made gratings with different widths and periods. The detailed fabrication process is provided in Materials and Methods.

In the first optical measurement, we aim to demonstrate that near-unity absorption can be achieved with our metasurface design. Given the presence of a reflective substrate, the absorptivity can be determined through measurement of the reflectivity $R(\lambda)$. We then also show a one-to-one correspondence between the features in the emissivity and absorption spectra. This facilitates an assignment of the various emission peaks to specific optical resonances through relatively simple simulations of the absorption spectrum. Last, we experimentally demonstrate dynamic emissivity control by electrical biasing.

We use a Fourier transform IR (FT-IR) microscope to obtain the reflectivity and thermal emissivity spectra (Fig. 2A). The black and red curves in Fig. 2B correspond to the reflectivity and emissivity, respectively, from a sample with 750-nm-wide strips spaced at a period of 1150 nm. We obtain both spectra by placing the sample on a hot plate at 200°C. The emissivity and reflectivity spectra show a number of complementary peaks and valleys at wavelengths around 5.4 and 7.9 μm. The absorptivity obtained by taking the complement of the reflectivity ($A = 1 - R$) is also compared to the emissivity in the Supplementary Materials (fig. S1), which confirms the reciprocal relationship (*11*, *17*).

To understand the origin of these spectral features, we analyze the device using electromagnetic simulations. Figure 2C shows the relative permittivity of the low-doped (n^+) and high-doped (n^{++}) InAs layers. The optical properties for each doping level are well described by the Drude model for the permittivity $\varepsilon = \varepsilon_{inf} - \omega_P^2/(\omega^2 + i\Gamma\omega)$, where ε_{inf} is the infinite-frequency permittivity, ω_P is the plasma frequency, ω is the angular frequency, and Γ is the carrier collision frequency. The plasma frequency is directly related to the mobile carrier concentration n by $\omega_P = [(ne^2)/(\varepsilon_0 m_e^*)]^{1/2}$, where e is the electron charge, ε_0 is the free-space electric permittivity, and m_e^* is the effective mass of the carriers. The permittivity of the high-doped (n^{++}) InAs layer (green curve) is positive for wavelengths below 4.8 μm, whereas it is negative above that wavelength. The ENZ wavelength for the low-doped (n^+) InAs layer (blue curve) is at 7.3 μm. The imaginary part of the dielectric constants is also provided in the Supplementary Materials (fig. S2).

The reflectivity spectrum simulated with the optical properties provided above (blue curve in Fig. 2B) agrees well with the reflectivity

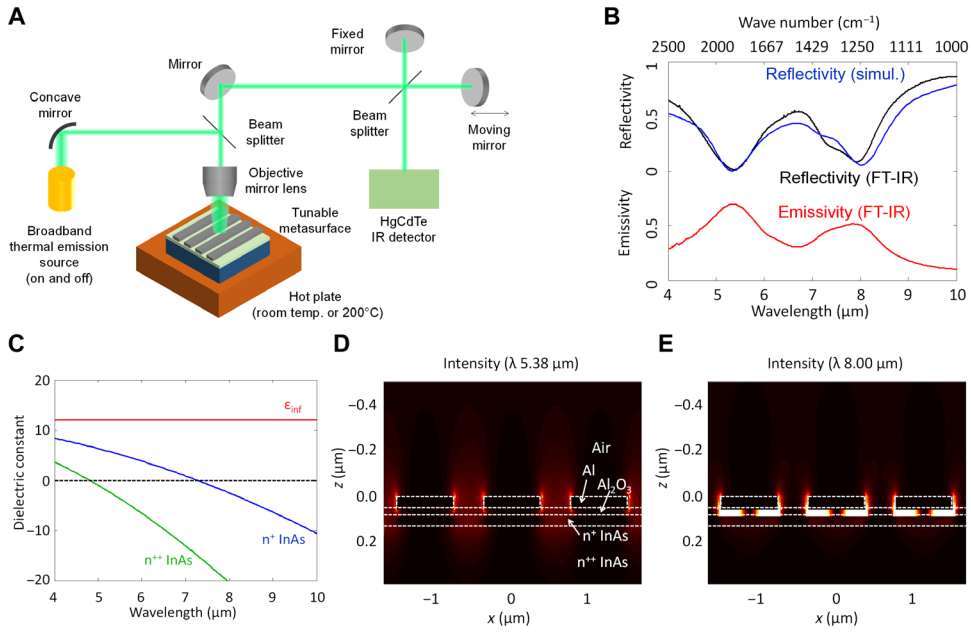

Fig. 2. Reciprocal relationship between the absorptivity and the emissivity. (**A**) FT-IR microscope with reflectivity and emissivity measurement modes. (**B**) Measured reflectivity (black curve) and emissivity at 200°C (red curve) spectra taken for a metasurface with 750-nm-wide strips spaced at a period of 1150 nm. The simulated reflectivity (blue curve) spectrum at normal incidence is shown. There are two reflection dips: a short wavelength dip around the wavelength of 5.4 μm and a long wavelength dip composed of two separate features centered around 7.2 and 8.0 μm. The reflectivity (black curve) dips and emissivity peaks coincide well with each other. (**C**) Real part of the dielectric constant (relative electric permittivity) of the low-doped (n^+; blue curve) InAs and high-doped (n^{++}; green curve) InAs layers and the infinite-frequency dielectric constant (ε_{inf}; red curve). (**D** and **E**) Electric field intensity distribution for normally incident illumination at wavelengths (λ) of 5.38 μm in (D) and 8.0 μm in (E).

measurement and shows two broad reflectivity dips. One dip occurs at a wavelength of 5.4 μm. From an analysis of the field distribution at this illumination wavelength (Fig. 2D), we link this feature to the impedance matching between the incident region (air) and the bottom n^{++} InAs layer. The dielectric constant of the n^{++} InAs layer is around unity around this wavelength. Other configurations composed of the Al gratings, the Al_2O_3 layer, and the n^+ InAs active layer are as thin as $^1/_{40}$ of the free-space wavelength. Consequently, the incident light passes those intermediate layers and gets absorbed in the impedance matched lossy region (bottom n^{++} InAs layer). This kind of reflectivity dip around a wavelength, where the real part of the permittivity is matched to the incident region, was also found and reported in (*33*). As the absorption occurs primarily in the n^{++} InAs layer (green curve in Fig. 2C), this is not tunable with external electrical bias, and the reflectivity dip at 5.4 μm is unaffected by the gating action.

Optical simulations indicate that the longer wavelength dip is composed of two closely spaced resonances located at the wavelengths of 7.2 and 8.0 μm and originating from gap plasmon modes with slightly different mode indices on either side of the ENZ wavelength. The electric field intensity distribution at the wavelength of 8.0 μm is depicted in Fig. 2E. The field is largely confined between the Al grating and the n^{++} InAs substrate. At this wavelength, the high-doped (n^{++}) InAs layer features a larger, negative dielectric constant of $\varepsilon = -20.3$ (green curve in Fig. 2C), allowing it to effectively push the fields into the gap. The gap plasmons can propagate in the waveguide formed by the top Al strip and the bottom mirror (leading to the propagation phase) and are reflected at the end facets of the Al strip (resulting in the reflection phase). When the total phase accumulation of the propagation and reflection phases becomes an integer multiple of 2π, resonance occurs (*30*). At such a resonance in the strip cavity, the absorption reaches a maximum and the measured reflectivity is minimized (*13*).

As a next step, we demonstrate dynamic thermal emission control by applying an electrical bias to the InAs-based metasurface. To prevent the formation of As_2O_3, which can occur above 300°C, we set the hot plate at a safe temperature of 200°C. The relatively low temperature used here decreases the overall radiation intensity from the metasurface (*4*). To enhance the signal-to-noise ratio in the measurement, we fabricated metasurfaces with relatively large surface areas (600 μm × 600 μm) (fig. S3). The electrical bias is applied through probe tips that contact the Al grating–based metasurface (fig. S3).

Figure 3 shows the measured emissivity (panel A) and reflectivity (panel B) spectra, as well as the simulated reflectivity spectrum (panel C). The red, green, and blue curves in each panel correspond to the cases of zero bias, negative bias for depletion, and positive bias for accumulation, respectively. The spectrum is shown from 6.6 to 7.8 μm, as only the features in the spectral range are affected by the external bias. The spectral position of the emissivity peak or reflectivity dip is determined by the Fabry-Pérot resonance condition for the gap plasmons, whose mode index is electrically tuned. Electron accumulation in the low-doped (n^+) active InAs layer via a positive gate bias (blue curves in Fig. 3, A to C) results in a blue shift of the resonance. This is because the increased plasma frequency leads to a decrease in the permittivity of the active layer, which, in turn, results in a decrease in the mode index of the gap plasmon (*29*). The depletion via a negative bias (green curves in Fig. 3, A to C) results in a red shift of the resonance. This originates from the fact that the permittivity of the active layer increases up to the magnitude of the infinity-frequency permittivity (ε_{inf}), giving rise to the higher mode index. The dielectric constant under applied bias and the resultant

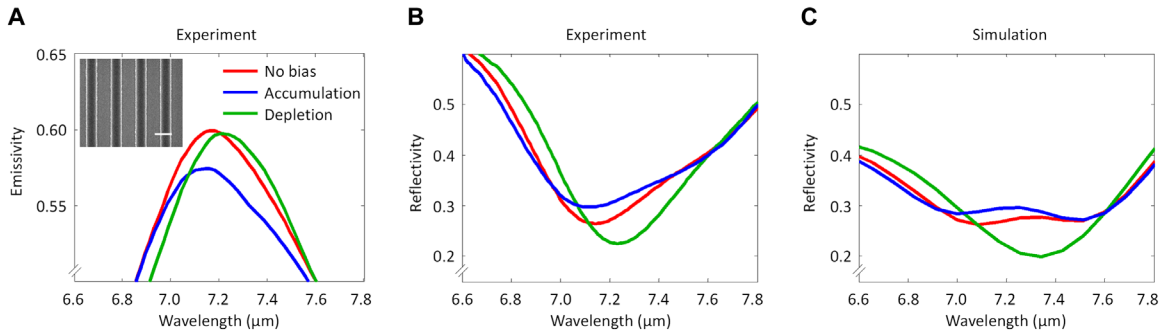

Fig. 3. Dynamic control of thermal emission and reflection from the InAs-based metasurface. (**A**) Emissivity spectrum for no bias (red curve), depletion (green curve), and accumulation (blue curve). For the depletion, a positive bias of +10 V was applied, and for the accumulation, a negative bias of −7 V was applied, for the sake of avoiding dielectric breakdown. The inset shows the SEM of the sample. Scale bar, 1 μm. The grating width and period are 590 nm and 1.4 μm, respectively. The sample area is 600 μm × 600 μm. The hot plate temperature is set to 200°C. (**B** and **C**) Reflectivity spectrum from experiment (B) and simulation (C) for no bias, depletion, and accumulation. The color notations are the same as in (A). The grating width and period are 545 and 1285 nm, respectively. A positive bias of +15 V and a negative bias of −15 V were used, respectively.

mode index change are provided in fig. S2, from which the aforementioned functional behavior can be inferred. The general working principle on the gate bias and the spectral shift of the resonance are similar to our previous report on a transparent conducting oxide (TCO)–based active tuning of a metasurface; more details can be found in (*27*).

Because of the blue and red shifts of the emissivity peaks, we can tailor the emissivity at a fixed wavelength. Figure 3A shows that at a wavelength of 7.3 μm, the absolute difference in the emissivity between the depletion (green) and accumulation (blue) conditions is 3.6%P ($\Delta E = E_{dep} - E_{acc}$), where E_{dep} and E_{acc} denote the emissivity of the depletion and the accumulation, respectively. The relative emissivity change ($\Delta E/E_{acc}$) is 6.5%. For the sake of comparison with previous results, we provide the measurement data in terms of various scales, including the emissivity (%), the emission intensity, the relative emissivity with E_{acc} being a criterion, and the relative emission intensity with E_{acc} being a criterion in the Supplementary Materials (fig. S4).

The magnitude of the emissivity change in the proposed configuration is limited by two factors, which are expected to be resolvable: one is stability of the electrical contact between the pad and probe tip, and the other is the long electromagnetic field tail into the high-doped bottom InAs layer. At room temperature, the dielectric strength of the Al_2O_3 layer was measured to be 7.3 million volts (MV) cm^{-1}, corresponding to a breakdown voltage of 20 V for the 30-nm layer used here. However, when the sample is placed on top of the 200°C hot plate, the likelihood that probe tips penetrate through the Al pads and gate oxides was found to be increased. As such, the dynamic emission control experiment was conducted with a maximum positive bias up to +10 V and a maximum negative bias down to −7 V. The dynamic reflection control experiment without the hot plate (fig. S5) showed that the modulation can be substantially enhanced when a higher bias (20 V) was applied. Therefore, it is expected that the change of the emissivity could be substantially increased with judiciously designed electrical contacts that might not suffer from these penetration issues. The second issue (deep penetration of electromagnetic field into the bottom InAs layer) originates from the fact that the absolute value of the real part of the negative dielectric constant of the high-doped bottom InAs layer (−14.46; Fig. 2C) is much smaller than that of Al (−4407; see Materials and Methods). Hence, the electromagnetic field of the gap plasmon (Fig. 2E) is not fully confined within the gate oxide and the low-doped active InAs layer. Instead, it holds a long tail (a 1/*e* decay length of 173 nm with a mode index of 5.6 + 1.8*i* at a wavelength of 7.2 μm) into the bottom InAs layer, which suffers from high dissipation loss. This limitation can be circumvented by using transfer and wafer bonding so that the active InAs layer is located on top of metal such as Al.

The thermal radiation generated from the metasurface in the presented linear grating configuration is polarized, with the electric field perpendicular to the grating. This is because the working principle of the devised configuration is through the excitation of gap plasmons between the top Al strips and the bottom high-doped InAs layer. The excitation of these plasmons is symmetry forbidden in the case where the light is polarized along the metallic strips. Figure 4A shows the emissivity spectrum measured through a polarizer with various orientation angles. The red curve corresponds to the electric field parallel to the grating (along the *y* axis), whereas the black curve shows the case where the electric field is perpendicular to the grating (along the *x* axis) (see inset to Fig. 4). The green and blue curves show the spectra for intermediate angles of 30° and 60° with regard to the Al gratings. The measured thermal emission reaches a maximum when the measurement polarization angle is oriented perpendicular to the strips in the grating (black curve). These measurements suggest that the emitted field is well polarized in accordance with the grating design. One can easily facilitate on-demand emission control of the polarization state as well by designing metasurfaces with more complicated patterns. Figure 4B shows the simulation results for the polarization-dependent thermal emission. The emission spectrum was obtained by calculating $1 - R(\lambda)$ for various polarizations and agrees well with the measured data.

One potential advantage of the proposed configuration is the high speed (*34*, *35*). Although a modulation speed measurement was not conducted in this study because the response time of the HgCdTe detector we used in the FT-IR was in the order of seconds, it is possible to estimate the performance based on the equivalent resistor-capacitor (RC) circuit modeling. Some of the current authors have carried out speed measurement on a tunable metasurface based on the TCOs and showed that the 3-dB cutoff frequency can be obtained from the RC time constant (*27*). As we apply this approach to the proposed configuration, the resistance is mainly governed by the top electrode (Al gratings) and the bottom ground layer (GaAs substrate). The resistance would be less than ~100 ohms. The DC permittivity of Al_2O_3 was measured

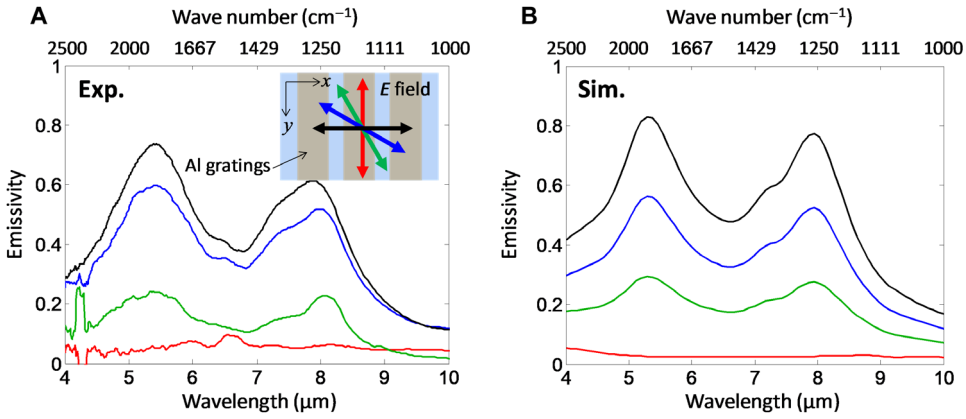

Fig. 4. Polarization property of emitted field from the metasurface comprising one-dimensional metallic gratings. A polarizer is inserted in front of the detector. Thermal emission spectra were measured for orientation polarizer angles of 0° (black curve), 30° (blue curve), 60° (green curve), and 90° (red curve), respectively. The inset in (**A**) shows a schematic diagram of the Al gratings along with *x* and *y* axes. The arrows denote the electric field orientations that can pass the polarizer. The grating width and period are 775 and 1150 nm, respectively, and the hot plate is set to 200°C. Simulation results in (**B**) show good agreement with the measured data.

to be around 7.44. The thickness of Al_2O_3 is 30 nm. As such, the capacitance of Al/Al_2O_3/InAs configuration is around 332 pF for a sample size of 600 μm × 600 μm, with a filling ratio of 0.42 (590-nm grating width over 1400-nm period in Fig. 3A) and 9.2 pF for the same filling ratio but a smaller sample size of 100 μm × 100 μm. Consequently, the 3-dB cutoff frequency would be similar to or larger than 4.8 MHz for a size of 600 μm × 600 μm and 172 MHz for a size of 100 μm × 100 μm. This modulation speed is similar to or slightly less than that previously reported in (*24*), where the operation speed of 600 kHz is experimentally demonstrated for a device with an area of 1.8 mm × 1.8 mm. We note that the modulation speed of voltage-controlled capacitive devices is mainly dependent on the RC time constant, and the capacitance is proportional to device size. Therefore, it is necessary to take the area into account when we compare the modulation speed. In this context, a modulation speed of 600 kHz of (*24*) would be normalized to 5.4 MHz for an area of 600 μm × 600 μm, as in our configuration. By using the same approach, 1-GHz estimation in (*22*), which was calculated for a device size of 300 μm × 300 μm, can be normalized to 250 MHz at an area of 600 μm × 600 μm. The modulation speed demonstration is left for future work by using high-speed detectors.

SUMMARY AND CONCLUSIONS

In conclusion, we demonstrate dynamic thermal emission control by using an electrically tunable metasurface with an active InAs semiconductor layer embedded in the strip plasmonic cavities. It is shown that the charge carrier change in the InAs layer under external bias can tailor the resonance condition of the strip cavities, which, in turn, leads to a spectral shift of the emissivity peak. An emissivity change of 3.6%P is achieved at a wavelength of 7.3 μm. It is noteworthy that the peak wavelength for the thermal emission modulation can also be tuned by changing the in-plane parameter, such as the width of the strip plasmonic cavities, which allows spatially varying emission wavelength tuning with a monolithic fabrication. Furthermore, each plasmonic cavity for thermal emission tuning can be separately addressed, thereby enabling the individual control. It should be pointed out that this individual control might not be achieved by using the photonic crystal (*24*) or a perforated conducting layer with a thick spacer layer (*23*). Future developments of this type of metasurface could facilitate high-speed modulation and steering of thermal emission. In addition, high-speed modulation of thermal emission combined with lock-in amplifier technologies may enable noise reduction in gas sensing (*36*). We believe that our proposed method may shed light on various applications, such as nonequilibrium heat processes, IR spectroscopy, chemical sensing, and biological analysis.

MATERIALS AND METHODS

Sample preparation

Molecular beam epitaxy (MBE) was used to grow a 500-nm-thick InAs layer with a high (n^{++}) doping concentration of 1.0×10^{20} cm^{-3}, followed by an additional MBE growth of a 50-nm-thick InAs layer with a low (n^{+}) doping concentration of 1.0×10^{19} cm^{-3}. The gate oxide of 30 nm Al_2O_3 was prepared by atomic layer deposition (ALD) with ~400 cycles of alternating trimethylaluminum (TMA) and H_2O pulses at a substrate temperature of 270°C. The estimated dose per cycle was 900 and 1200 liters for TMA and H_2O, respectively, and the chamber pressure was maintained at 0.68 torr by continuous flow of dry N_2. A TMA predosing step consisting of 20 alternating TMA pulsing and N_2 purging cycles was performed before the main ALD process (*37*). This predosing step can lead to a better oxide quality by reducing the interface defect density, because TMA plays a role in passivating dangling bonds at the InAs-Al_2O_3 interface. The surface of the substrate can also be smoothened by having a thin monolayer of TMA without losing desirable electrical property. The top Al gratings were fabricated by standard e-beam lithography and e-beam deposition, followed by a liftoff process.

Optical and electrical characterization

The measurement setup was designed to switch the optical beam path between two modes: one for the reflection mode with a broadband thermal emission source turned on (hot plate turned off) and the beam splitter on top of the tunable metasurface, and the other for the thermal emission mode without the beam splitter and the hot plate turned on. The intensity pattern originating from the interference between the reflected light from a fixed mirror and one from the moving mirror was recorded in a HgCdTe (MCT) IR detector. The Fourier transformed signal reveals the spectral information from the tunable metasurface.

For the thermal emission measurement, we prepared two regions: One was covered by Al pad near the Al grating metasurfaces, which was used as the normalization, and the other was painted with carbon black, heat-safe paint. For a given sample having certain width and period of the Al gratings, electrical bias, and hot plate temperature, the four FT-IR spectra were recorded: I_{sample} (signal from a sample), I_{Al} (signal from the mirror-like Al pad), I_{carbon} (signal from the carbon paint region), and $I_{background}$ (signal from out-focused from the sample plane, measuring the background signal). The emission intensity was $I_{sample} - I_{Al}$. The block body radiation was $I_{carbon} - I_{background}$. The emissivity was then given by $(I_{sample} - I_{Al})/(I_{carbon} - I_{background})$.

Regarding the electrical properties of the Al_2O_3 layer, the DC permittivity (ε_{DC}) was measured to be 7.74 via a capacitance-voltage (CV) measurement (fig. S6). We performed current-voltage (IV) measurements to characterize a dielectric strength (E_{BD}, breakdown electric field) of 7.3 MV cm^{-1} (fig. S7).

Numerical simulation

The rigorous coupled-wave analysis (RCWA) was used for the full-field electromagnetic calculation. The number of the Fourier harmonics was set to 101, which was confirmed to be large enough to reach convergence. The refractive index of the Al_2O_3 layer was obtained by using ellipsometry (fig. S8). The refractive index of Al was chosen from the literature (*38*). The dielectric constant of the InAs layers was described by the Drude model. The effective electron mass for the high-doped InAs was 0.17 m_e, leading to a plasma frequency of 1.37×10^{15} rad/s. The effective electron mass at the band edge was 0.027 m_e (*39*), and that of the low-doped (n^+) InAs layer was obtained as 0.039 m_e by using a linear interpolation between the high-doped InAs and the band edge, which leads to a plasma frequency of 9.0×10^{14} rad/s. The collision frequency was determined by finding the best agreement with the experimental measurement. Physically reasonable values consistent with previous literature (*34*) of 2.0×10^{13} rad/s for the low-doped InAs and 5.0×10^{13} rad/s for the high-doped InAs were obtained, respectively. The infinite-frequency permittivity for both InAs layers was 12, which was obtained from the literature (*40*). The depletion layer at a bias of 0 V, 24.5 nm in the top (near Al_2O_3) n^+ InAs layer and 24 nm in the bottom (near n^{++} InAs) layer, was formed. Under a negative bias of −15 V, the depletion layer thickness was 1.5 nm. A positive bias with +15 V induced the formation of an accumulation layer with a thickness of 0.5 nm and an increase in the plasma frequency of 9.2×10^{14} rad/s while maintaining the collision frequency. The plasma frequency at the positive bias and the depletion and accumulation layer thicknesses were adjusted to reproduce the experimental results for various grating geometries. The comparison between the reflection measurement (FT-IR) and simulation (RCWA) for various grating widths and periods confirmed the agreement (figs. S9 and S10).

SUPPLEMENTARY MATERIALS

Supplementary material for this article is available at http://advances.sciencemag.org/cgi/content/full/4/12/eaat3163/DC1

Section S1. Comparison of the spectral absorptivity and emissivity

Section S2. Real and imaginary parts of the dielectric constants of the n^+ and n^{++} InAs layers and the mode index

Section S3. Photographs and SEM images of the samples for the tunable thermal emission measurements

Section S4. Various scales for emissivity changes (absolute and relative plots)

Section S5. Reflectivity tuning as a function of incremental electrical bias and the mode index

Section S6. Electrical characterization of the gate oxide Al_2O_3 (IV and CV)

Section S7. Refractive index of Al_2O_3 in mid-IR regime measured using ellipsometry

Section S8. Reflectivity tuning from samples with various widths and periods

Fig. S1. Comparison of the spectral absorptivity and emissivity.

Fig. S2. Optical properties of the switching materials and gap plasmon resonator.

Fig. S3. Optical microscopy and SEM images of the sample used for the tunable thermal emission measurement.

Fig. S4. Dynamic control of thermal emission in various scales.

Fig. S5. Tuning reflectivity with higher bias.

Fig. S6. Capacitance-voltage measurement of Al_2O_3.

Fig. S7. Dielectric strength measurements.

Fig. S8. Refractive index of Al_2O_3.

Fig. S9. Optical and SEM images of the sample for the reflectivity measurement.

Fig. S10. Reflectivity from samples with various grating widths.

REFERENCES AND NOTES

1. J. A. Schuller, T. Taubner, M. L. Brongersma, Optical antenna thermal emitters. *Nat. Photonics* **3**, 658–661 (2009).
2. T. Inoue, M. De Zoysa, T. Asano, S. Noda, Realization of narrowband thermal emission with optical nanostructures. *Optica* **2**, 27–35 (2015).
3. S. V. Boriskina, J. K. Tong, W.-C. Hsu, B. Liao, Y. Huang, V. Chiloyan, G. Chen, Heat meets light on the nanoscale. *Nanophotonics* **5**, 134–160 (2016).
4. B. E. A. Saleh, M. C. Teich, *Fundamentals of Photonics* (Wiley-Interscience, ed. 2, 2007).
5. P. J. Hesketh, J. N. Zemel, B. Gebhart, Organ pipe radiant modes of periodic micromachined silicon surfaces. *Nature* **324**, 549–551 (1986).
6. J.-J. Greffet, R. Carminati, K. Joulain, J.-P. Mulet, S. Mainguy, Y. Chen, Coherent emission of light by thermal sources. *Nature* **416**, 61–64 (2002).
7. C. Arnold, F. Marquier, M. Garin, F. Pardo, S. Collin, N. Bardou, J.-L. Pelouard, J.-J. Greffet, Coherent thermal infrared emission by two-dimensional silicon carbide gratings. *Phys. Rev. B* **86**, 035316 (2012).
8. N. Dahan, A. Niv, G. Biener, Y. Gorodetski, V. Kleiner, E. Hasman, Enhanced coherency of thermal emission: Beyond the limitation imposed by delocalized surface waves. *Phys. Rev. B* **76**, 045427 (2007).
9. A. P. Raman, M. A. Anoma, L. Zhu, E. Rephaeli, S. Fan, Passive radiative cooling below ambient air temperature under direct sunlight. *Nature* **515**, 540–544 (2014).
10. O. Ilic, P. Bermel, G. Chen, J. D. Joannopoulos, I. Celanovic, M. Soljačić, Tailoring high-temperature radiation and the resurrection of the incandescent source. *Nat. Nanotechnol.* **11**, 320–324 (2016).
11. J.-J. Greffet, M. Nieto-Vesperinas, Field theory for generalized bidirectional reflectivity: Derivation of Helmholtz's reciprocity principle and Kirchhoff's law. *J. Opt. Soc. Am. A* **15**, 2735–2744 (1998).
12. N. I. Landy, S. Sajuyigbe, J. J. Mock, D. R. Smith, W. J. Padilla, Perfect metamaterial absorber. *Phys. Rev. Lett.* **100**, 207402 (2008).
13. N. Liu, M. Mesch, T. Weiss, M. Hentschel, H. Giessen, Infrared perfect absorber and its application as plasmonic sensor. *Nano Lett.* **10**, 2342–2348 (2010).
14. M. A. Kats, F. Capasso, Optical absorbers based on strong interference in ultra-thin films. *Laser Photon. Rev.* **10**, 735–749 (2016).
15. D. L. C. Chan, M. Soljačić, J. D. Joannopoulos, Thermal emission and design in 2D-periodic metallic photonic crystal slabs. *Opt. Express* **14**, 8785–8796 (2006).
16. M. Ghebrebrhan, P. Bermel, Y. X. Yeng, I. Celanovic, M. Soljačić, J. D. Joannopoulos, Tailoring thermal emission via *Q* matching of photonic crystal resonances. *Phys. Rev. A* **83**, 033810 (2011).
17. X. Liu, T. Tyler, T. Starr, A. F. Starr, N. M. Jokerst, W. J. Padilla, Taming the blackbody with infrared metamaterials as selective thermal emitters. *Phys. Rev. Lett.* **107**, 045901 (2011).
18. D. Constantini, A. Lefebvre, A.-L. Coutrot, I. Moldovan-Doyen, J.-P. Hugonin, S. Boutami, F. Marquier, H. Benisty, J.-J. Greffet, Plasmonic metasurface for directional and frequency-selective thermal emission. *Phys. Rev. Appl.* **4**, 014023 (2015).
19. H. T. Miyazaki, T. Kasaya, H. Oosato, Y. Sugimoto, B. Choi, M. Iwanaga, K. Sakoda, Ultraviolet-nanoimprinted packaged metasurface thermal emitters for infrared CO_2 sensing. *Sci. Technol. Adv. Mater.* **16**, 035005 (2015).
20. X. Liu, W. J. Padilla, Dynamic manipulation of infrared radiation with MEMS metamaterials. *Adv. Opt. Mater.* **1**, 559–562 (2013).
21. S. Vassant, I. M. Doyen, F. Marquier, F. Pardo, U. Gennser, A. Cavanna, J. L. Pelouard, J. J. Greffet, Electrical modulation of emissivity. *Appl. Phys. Lett.* **102**, 081125 (2013).
22. S. Vassant, A. Archambault, F. Marquier, F. Pardo, U. Gennser, A. Cavanna, J. L. Pelouard, J. J. Greffet, Epsilon-near-zero mode for active optoelectronic devices. *Phys. Rev. Lett.* **109**, 237401 (2012).
23. V. W. Brar, M. C. Sherrott, M. S. Jang, S. Kim, L. Kim, M. Choi, L. A. Sweatlock, H. A. Atwater, Electronic modulation of infrared radiation in graphene plasmonic resonators. *Nat. Commun.* **6**, 7032 (2015).
24. T. Inoue, M. De Zoysa, T. Asano, S. Noda, Realization of dynamic thermal emission control. *Nat. Mater.* **13**, 928–931 (2014).

25. T. Inoue, M. De Zoysa, T. Asano, S. Noda, Electrical tuning of emissivity and linewidth of thermal emission spectra. *Phys. Rev. B* **91**, 235316 (2015).
26. R. Liu, Y. Zhong, L. Yu, H. Kim, S. Law, J.-M. Zuo, D. Wasserman, Mid-infrared emission from In(Ga)Sb layers on InAs(Sb). *Opt. Express* **22**, 24466–24477 (2014).
27. J. Park, J.-H. Kang, X. Liu, M. L. Brongersma, Electrically tunable epsilon-near-zero (ENZ) metafilm absorbers. *Sci. Rep.* **5**, 15754 (2015).
28. Y.-W. Huang, H. W. H. Lee, R. Sokhoyan, R. A. Pala, K. Thyagarajan, S. Han, D. P. Tsai, H. A. Atwater, Gate-tunable conducting oxide metasurfaces. *Nano Lett.* **16**, 5319–5325 (2016).
29. J. Park, J.-H. Kang, S. J. Kim, X. Liu, M. L. Brongersma, Dynamic reflection phase and polarization control in metasurfaces. *Nano Lett.* **17**, 407–413 (2017).
30. Y. C. Jun, J. Reno, T. Ribaudo, E. Shaner, J.-J. Greffet, S. Vassant, F. Marquier, M. Sinclair, I. Brener, Epsilon-near-zero strong coupling in metamaterial-semiconductor hybrid structures. *Nano Lett.* **13**, 5391–5396 (2013).
31. T. Søndergaard, S. I. Bozhevolnyi, Strip and gap plasmon polariton optical resonators. *Phys. Status Solidi B Basic Solid State Phys.* **245**, 9–19 (2008).
32. X. Liu, J.-H. Kang, H. Yuan, J. Park, S. J. Kim, Y. Cui, H. Y. Hwang, M. L. Brongersma, Electrical tuning of a quantum plasmonic resonance. *Nat. Nanotechnol.* **12**, 866–870 (2017).
33. S. Law, D. C. Adams, A. M. Taylor, D. Wasserman, Mid-infrared designer metals. *Opt. Express* **20**, 12155–12165 (2012).
34. M. Wagner, A. S. McLeod, S. J. Maddox, Z. Fei, M. Liu, R. D. Averitt, M. M. Fogler, S. R. Bank, F. Keilmann, D. N. Basov, Ultrafast dynamics of surface plasmons in InAs by time-resolved infrared nanospectroscopy. *Nano Lett.* **14**, 4529–4534 (2014).
35. A. G. Milnes, A. Y. Polyakov, Indium arsenide: A semiconductor for high speed and electro-optical devices. *Mater. Sci. Eng. B* **18**, 237–259 (1993).
36. P. M. Maya-Hernández, L. C. Álvarez-Simón, M. T. Sanz-Pascual, B. Calvo-López, An integrated low-power lock-in amplifier and its application to gas detection. *Sensors* **14**, 15880–15899 (2014).
37. J. Ahn, T. Kent, E. Chagarov, K. Tang, A. C. Kummel, P. C. McIntyre, Arsenic decapping and pre-atomic layer deposition trimethylaluminum passivation of Al_2O_3/InGaAs(100) interfaces. *Appl. Phys. Lett.* **103**, 071602 (2013).
38. E. D. Palik, *Handbook of Optical Constants of Solids* (Academic Press, 1985).
39. M. Cardona, Electron effective masses of InAs and GaAs as a function of temperature and doping. *Phys. Rev.* **121**, 752–758 (1961).
40. O. G. Lorimor, W. G. Spitzer, Infrared refractive index and absorption of InAs and CdTe. *J. Appl. Phys.* **36**, 1841–1844 (1965).

Acknowledgments: We thank E. Hasman for the helpful discussion and suggestion. We are also grateful to R. Synowicki for optical characterization of the Al_2O_3. J.P. appreciates S. Kim's support and assistance. **Funding:** We would like to acknowledge funding from the Department of Energy (grant DE-FG07-ER46426), the Global Climate and Energy Project, and a Multidisciplinary University Research Initiative from the Air Force Office of Scientific Research (AFOSR MURI award no. FA9550-12-1-0488). **Author contributions:** J.P., J.-H.K., S.R.B., and M.L.B. conceived the ideas for this research project. J.P., J.-H.K., and X.L. developed the theoretical prediction. J.P. designed the sample. S.J.M. and S.R.B. fabricated the low- and high-doped InAs layers. K.T. and P.C.M. prepared and characterized the gate oxide. J.-H.K. measured and characterized optical response. J.P. conducted electrical characterization. J.P., J.-H.K., and M.L.B. prepared the manuscript. M.L.B. supervised the project. All authors discussed the manuscript and agreed on its final content. **Competing interests:** The authors declare that they have no competing interests. **Data and materials availability:** All data needed to evaluate the conclusions in the paper are present in the paper and/or the Supplementary Materials. Additional data related to this paper may be requested from the authors. All data, analysis details, and material recipes presented in this work are available upon request to M.L.B.

Submitted 13 February 2018
Accepted 7 November 2018
Published 7 December 2018
10.1126/sciadv.aat3163

Citation: J. Park, J.-H. Kang, X. Liu, S. J. Maddox, K. Tang, P. C. McIntyre, S. R. Bank, M. L. Brongersma, Dynamic thermal emission control with InAs-based plasmonic metasurfaces. *Sci. Adv.* **4**, eaat3163 (2018).

Dynamic thermal emission control with InAs-based plasmonic metasurfaces

Junghyun Park, Ju-Hyung Kang, Xiaoge Liu, Scott J. Maddox, Kechao Tang, Paul C. McIntyre, Seth R. Bank and Mark L. Brongersma

Sci Adv **4** (12), eaat3163.
DOI: 10.1126/sciadv.aat3163